GEOCHRONOMETRIA 53 (2026) 241920
DOI 10.20858/geochr/241920



Available online at https://www.geochronometria.com/

Conference Proceedings of the 7th Asia Pacific Luminescence and Electron Spin Resonance Dating Conference
21-24 September, 2025, Jeju, Korea
Guest Editor: Tae-Ho Lee

LATE QUATERNARY SLIP RATE AND GEOMETRIC SEGMENTATION OF THE NORTHERN ULSAN FAULT IN SOUTHEASTERN KOREA: INSIGHTS FROM OFFSET ALLUVIAL FANS AND LUMINESCENCE DATING

SU-HO JEONG[1], JEONG-SIK OH[2], SEONGCHAN HONG[3], KIWOONG PARK[1], SANGYEOL BAE[1] and YOUNG-SEOG KIM[1]

[1]Division of Earth and Environmental System Sciences, Pukyong National University, Busan 48513, Republic of Korea
[2]Department of Geography, Kyungpook National University, Daegu 41566, Republic of Korea
[3]Department of Geography Education, Korea National University of Education, Cheongju 28173, Republic of Korea

Received 2 February 2026 Accepted 19 October 2026

Abstract
Constraining the long-term activity of reverse faults in intraplate regions is challenging due to subtle surface expressions and limited paleoseismological records. This study investigates the late Quaternary activity of the Galgok fault (GF), located in the northern part of the Ulsan Fault, through geomorphic mapping and luminescence dating of offset alluvial fan surfaces. Detailed geomorphic analysis identified multiple generations of alluvial fans and fault-related markers, enabling measurement of cumulative vertical offsets. Quartz OSL dating of the Qf_2 surface yielded formation ages ranging from 7.6 ± 0.6 to 34 ± 3 ka, while K-feldspar $pIRIR_{50,225}$ dating constrained the older Qf_3 surface to 175 ± 6 ka. Vertical slip rates were estimated using Monte Carlo simulations that propagate uncertainties in both offset and age. Based on a cumulative vertical offset of 3.31 ± 0.24 m, late Quaternary time-averaged vertical slip rates range from 0.1 to 0.44 mm/yr, depending on the Qf_2 age. Excluding a potentially reworked near-surface sample yields a more conservative range of 0.1 to 0.21 mm/yr. Geometric analysis indicates that the GF constitutes a single geometric segment (4.56 km). These results demonstrate the effectiveness of combining geomorphic markers with luminescence dating for assessing long-term fault behavior in low-strain intraplate settings.

Keywords
Active reverse fault, luminescence dating, alluvial fan, slip rate, geometric segmentation

1. Introduction

Earthquakes commonly occur through the reactivation of pre-existing geological structures, particularly active faults (Sibson, 1985; Kim and Sanderson, 2008). Accordingly, characterizing the spatial distribution and activity history of active faults is essential for effective earthquake hazard mitigation. Earthquakes occurring on unmapped faults may cause disproportionately large damage, even when their magnitudes are moderate. In particular, the geomorphological and stratigraphic expressions associated with reverse faults tend to be subtle and geometrically complex (McCalpin, 2009), making their identification and characterization challenging. In many cases, the presence and geometry of reverse faults are not fully recognized until a

Corresponding author: Y.-S Kim
e-mail: ysk7909@pknu.ac.kr

ISSN 1897-1695 (online), 1733-8387 (print)
© 2026 S.-H. Jeong *et al.* This work is licensed under the **CC-BY 4.0** License.

large earthquake occurs (e.g., Ma *et al*., 1999; Burchfiel *et al*., 2008; Kaneda *et al*., 2008).

Reverse faults constitute one of the major fault types in compressional tectonic settings. Given that the Korean Peninsula is characterized by a compressional stress regime within a low-strain intraplate setting (Park *et al*., 2007; Soh *et al*., 2018) (**Fig. 1a**), understanding the long-term spatiotemporal characteristics of reverse faults is of fundamental importance. The Ulsan Fault, together with the Yangsan Fault, is recognized as one of the principal active reverse faults extending in a north-south direction across the southeastern Korean Peninsula (**Fig. 1b**). In the vicinity of these fault systems, major industrial facilities, including nuclear power plants, are densely distributed, along with large metropolitan areas such as Busan, Ulsan, and Pohang, which together host populations of several million. Owing to these geographic and societal conditions, seismic hazard associated with fault systems in southeastern Korea is regarded as an issue of national significance. In particular, the successive occurrence of the 2016 Gyeongju earthquake (Woo *et al*., 2019) and the 2017 Pohang earthquake (Kim *et al*., 2018) highlighted the need for a more comprehensive understanding of earthquake generation and active fault behavior in southeastern Korea, including the Ulsan Fault.

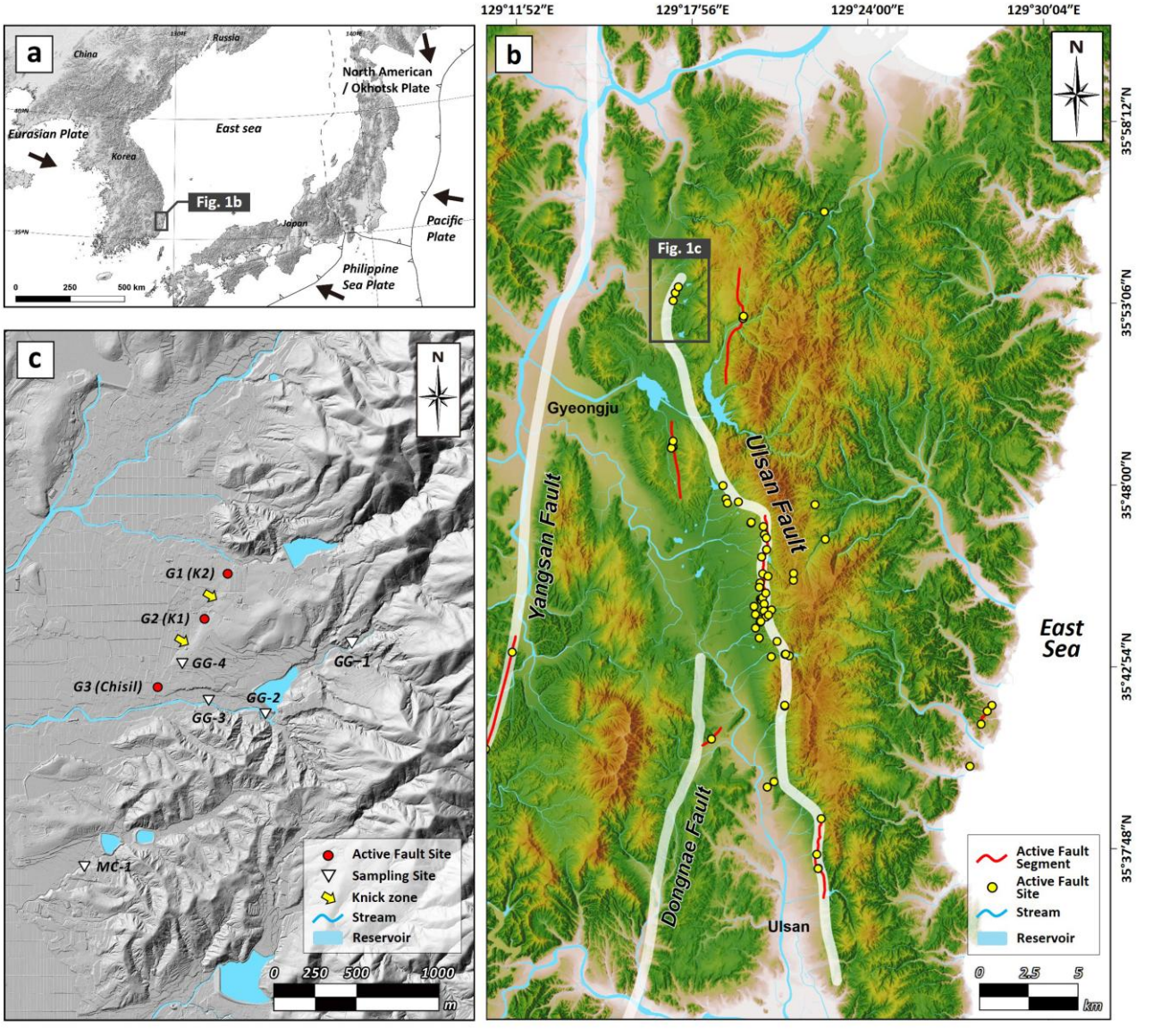


Fig. 1. *(a) Tectonic map of the region surrounding the Korean Peninsula. (b) Geomorphic map showing the regional distribution of the major faults in SE Korea, including Ulsan, Yangsan, and Dongnae faults. (c) Generalized topography of the study area showing previously reported active fault sites, luminescence sampling sites, and knickzones.*

Although detailed investigations of the Ulsan Fault have been conducted as part of the Korea Active Fault Mapping Project (KAFMP), through which multiple active faults were identified and new fault segments were delineated (Kim *et al*., 2022) (**Fig. 1b**), previous studies have predominantly focused on its central and southern parts (e.g., Choi *et al*., 2012; Kim *et al*., 2022). Consequently, the northern sector remains comparatively poorly constrained, despite the occurrence of previously identified Quaternary faulting and the potential importance of this sector for understanding the along-strike continuity and long-term deformation of the Ulsan Fault.

Several studies have documented the Galgok Fault (GF) in the northern part of the Ulsan Fault (Okada *et al*., 1999, 2001; Suzuki *et al*., 2005; Inoue and Choi, 2006; Kyung and Lee, 2006; Kee *et al*., 2009; Choi *et al*., 2012; Kim *et al*., 2022). Trench investigations conducted along a well-defined fault scarp exposed fault structures at the G1 (K2) (Suzuki *et al*., 2005), G2 (K1) (Okada *et al*., 1999, 2001), and G3 (Chisil) (Inoue and Choi, 2006) trench sites (**Fig. 1c**). These studies documented repeated Quaternary activity of the GF and demonstrated its relevance to the tectonic evolution of the Ulsan Fault (**Tables 1–2**). Despite evidence for repeated Quaternary activity, several fundamental aspects of the GF remain inadequately characterized. First, the surface continuity and geometric expression of the GF remain poorly constrained. Although surveys of the GF were carried out as part of the KAFMP, the spatial extent of the GF has not been clearly delineated (e.g., Kim *et al*., 2022). In particular, the lack of Light Detection and Ranging (LiDAR) data has posed a major limitation on detailed mapping of surface geomorphic features, which are critical for tracing the along-strike continuity of the fault. Second, estimates of cumulative displacement along the GF remain poorly constrained. Multiple trench investigations failed to identify bedrock on both the hanging wall and footwall, thereby preventing reliable quantification of long-term displacement. Third, robust chronological constraints are either uncertain or lacking. Although radiocarbon dating was applied to trench exposures, systematic age reversals have been reported (e.g., Okada *et al*., 1999, 2001; Inoue and Choi, 2006; Kyung, 2007; Kee *et al*., 2009). Furthermore, the formation ages of Quaternary geomorphic surfaces within the study area have not yet been constrained using independent numerical dating methods. Luminescence dating has been widely applied to

Table 1. *Sedimentary and age constraints from previous trench profiles of the Galgok Fault (GF).*

Fault	Unit	Stratigraphic layer Description	^{14}C Age (yr B.P.)	References
G1	I	Topsoil	-	Suzuki *et al.* (2005); Kyung (2007)
	II	AT tephra*-bearing loess	1,560 ± 60 (upper bed)	
	III	Alluvial fan deposit	14,010 ± 240; 13,760 ± 140 (lower bed)	
	IV-VIII	Alluvial fan deposit	25,750 ± 240	
G2	I	Topsoil	-	Okada *et al.* (1999, 2001); Kyung (2007)
	II	Fresh gravel with brownish soil	Modern	
	III	Loess	23,210 ± 460	
	IV	Orange-colored soil	-	
	V	Reddish soil	21,440 ± 430	
	VI-VII	Slightly to highly weathered gravel	-	
G3	-	Topsoil	-	Inoue and Choi (2006); Kee *et al.* (2009)
	KB	Silt with granule	10,580 ± 50; 7,910 ± 50; 1,440 ± 50	
	KC	Sand with granule to pebble	4,930 ± 40; 2,840 ± 40	
	KDa	Gravel with granule	-	
	KDb	Granule with cobble	-	
	KDc	Silt with granule	-	
	KDd	Alternation granule and pebble	9,480 ± 50	

** The AT tephra has an age of approximately 25 ka*

Table 2. *Previously reported fault geometry, kinematics, and cumulative displacement of the Galgok Fault (GF).*

Fault	Strike	Dip	Kinematics	Cumulative displ. (m)*	Reference layer	References
G1	N20°W	18-40°NE	Reverse	2.5	VI	Suzuki *et al.* (2005); Kyung (2007)
G2 F1	N50°E	70°SE	Reverse			Okada *et al.* (1999, 2001); Kyung (2007)
G2 F2	N9°E	38°SE	Reverse	1.8–2.4	V	
G3 FA	N20°W	60°NE	Reverse			Inoue and Choi (2006); Kee *et al.* (2009)
G3 FB	N20°W	30°NE	Reverse	2.0	KDd	

** Apparent dip separation*

alluvial and fluvial deposits associated with displaced geomorphic surfaces, providing numerical age constraints that, when appropriately linked to the geomorphic markers, can be used to evaluate long-term fault activity and slip rates (Cheong *et al*., 2003; Rizza *et al*., 2011; Gong *et al*., 2017).

Although no moderate-to-large earthquakes, or events clearly attributed to the GF, have been documented within the study area based on instrumental and historical records (KMA, 2012, 2026), the absence of recorded seismicity does not necessarily indicate fault inactivity. In slow-deforming intraplate regions, faults commonly exhibit long recurrence intervals, making it difficult to evaluate their activity using short-term seismic observations alone. Consequently, geomorphological and geochronological investigations provide essential information for assessing long-term fault behavior (Wallace, 1977; McCalpin, 2009).

To overcome these limitations, this study combines high-resolution LiDAR-based geomorphic mapping, fault-scarp analysis, and luminescence dating of displaced alluvial fan deposits. Specifically, this study aims to: (1) map the along-strike continuity and geometric characteristics of the GF using detailed geomorphic analyses; (2) quantify cumulative vertical displacement along the fault based on displaced geomorphic markers; (3) constrain the formation ages of faulted alluvial fan surfaces using quartz and K-feldspar luminescence dating; and (4) estimate the late Quaternary slip rate of the GF and evaluate its implications for the long-term behavior and geometric segmentation of the northern Ulsan Fault. By integrating fault-trace mapping, cumulative displacement measurements, and luminescence chronologies, this study also evaluates how variations in fault continuity and displacement distribution reflect the long-term slip behavior and geometric segmentation of the GF. The results provide the first integrated geomorphic and geochronological constraints on the activity, slip rate, and geometric segmentation of the GF, thereby improving our understanding of reverse fault deformation and seismic hazard in the southeastern Korean Peninsula.

2. Geological Setting and Study Area

The tectonic framework of the Korean Peninsula is governed by complex interactions among surrounding tectonic plates, including the subduction of the Philippine Sea Plate and the Pacific Plate beneath the Eurasian Plate, as well as far-field stresses associated with the collision between the Indian and Eurasian plates (Park *et al*., 2006; Kim *et al*., 2016; Kuwahara *et al*., 2021) (**Fig. 1a**). During the Cenozoic, deformation of the Korean Peninsula-particularly in its southeastern region-was strongly influenced by the initiation of the India-Eurasia collision at approximately 50 Ma and by the opening and subsequent closing of the East Sea (Sea of Japan), which began around 25 Ma (Tapponnier and Molnar, 1976; Hall, 2002; Fournier *et al*., 2004). Since the Pliocene, the regional stress regime has shifted to a compressional setting characterized by an E-W to ENE-WSW-oriented maximum horizontal stress (N70°-75°E), which is considered to have persisted to the present. This stress configuration has been documented through multiple lines of evidence, including fault-slip data (Park *et al*., 2007; Kim *et al*., 2016), focal mechanism solutions (Soh *et al*., 2018; Kuwahara *et al.*, 2021), and borehole data (Kim *et al*., 2021). Temporal changes in the regional stress regime have played a critical role in the development and kinematic evolution of the Ulsan Fault. The Ulsan Fault initially experienced dominant normal and strike-slip motion; however, since the Pliocene, it has undergone oblique-slip deformation with a predominant reverse-slip component, reflecting a history of polyphase deformation. Such kinematic evolution is interpreted as the result of reactivation of pre-existing geological structures under changing stress conditions (Kim *et al*., 2016).

The study area is located in Galgok-ri, Gyeongju City, within the northern part of the Ulsan Fault (**Fig. 1**). This area has previously been described either as part of the northern Ulsan Fault (e.g., Okada *et al*., 1999, 2001; Suzuki *et al*., 2005; Inoue and Choi, 2006; Kyung and Lee, 2006; Kee *et al*., 2009; Choi *et al*., 2012; Kim *et al*., 2020) and/or as the southwestern margin of the Miocene Pohang Basin, specifically the Bomun sub-basin (e.g., Park, 2004; Song *et al*., 2022). Multiple alluvial fans are developed in the study area, and distinct linear knickpoints are well preserved on the fan surfaces (Okada *et al*., 1999, 2001) (**Fig. 1c**). These geomorphic characteristics make the study area particularly suitable for addressing the principal uncertainties identified in previous studies of the GF. The preservation of fault-related geomorphic markers across multiple alluvial fan surfaces allows the surface continuity of the fault to be traced and cumulative vertical displacement to be quantified. In addition, the alluvial fan deposits provide suitable sedimentary archives for luminescence dating, enabling independent numerical constraints on the depositional ages of the geomorphic surfaces associated with fault deformation. Thus, the study area provides a suitable setting for integrating geomorphic mapping, displacement measurements, and luminescence dating to evaluate the long-term activity of the GF.

3. Method

3.1. Geomorphic Mapping and Quantification of Fault Scarps

Based on field surveys and GIS analysis of high-resolution (0.5 m spatial resolution) LiDAR data, lineaments crossing the fault sites (G1, G2, and G3) were identified, and alluvial fans within the study area were systematically mapped. Lineaments were traced primarily using distinct fault-related geomorphic markers, such as fault scarps and offset surface structures that directly reflect surface deformation. In areas where the original topography has been substantially modified by anthropogenic activities (e.g., agriculture), the delineation of lineaments was supplemented using previously published datasets (Okada *et al*., 1999, 2001; Inoue and Choi, 2006; Choi *et al*., 2012; Kim *et al*.,

2022) and historical aerial photographs acquired in 1954 and 1968. Alluvial fans were classified into three geomorphic surfaces (Qf_1-Qf_3) based on their relative elevation above the present channel bed and stratigraphic characteristics. Qf_1 occurs at 2.0-6.5 m above the present channel bed, Qf_2 at 7.5-18.0 m, and Qf_3 at ≥20.5 m. Accordingly, Qf_1, Qf_2, and Qf_3 represent the lower, intermediate, and higher alluvial fan surfaces, respectively.

To quantify the vertical offset of fault-generated scarps, five topographic profiles were established at each of the two fault sites (G1 and G2). The profiles were oriented to traverse the faults while accounting for the strike range of the lineaments (N20°–30°E), with azimuths varied at 2.5° intervals. Along each profile, elevation values were sampled at 1-m spacing. For each distance x_i, the five elevation values were averaged to construct a mean elevation profile.

The mean elevation profile was divided into two segments relative to the fault position (x=150 m): the foreland segment (0–150 m) and the hinterland segment (150–300 m). Linear regressions were applied independently to each segment. Data affected by artificial structures (66–95 m in G2) were excluded from the regression analysis. The relationship between distance x and mean elevation y in each segment was approximated by a first-order linear function, and the scarp height D produced by faulting was defined as the difference between the predicted elevations of the two regression lines at x = 150 m:

$$D = | \hat{y}_2(150) - \hat{y}_1(150) |.$$

The uncertainty of the predicted elevation at a given position x_0 was estimated using the 95% confidence interval of the linear regression:

$$\hat{y}(x_0) \pm t_{n-2,\,0.975} \cdot s \cdot \sqrt{\frac{1}{n} + \frac{(x_0 - \bar{x})^2}{\sum (x_i - \bar{x})^2}},$$

where n is the number of samples, $\bar{x}$ is the mean of x, s is the standard error of the regression residuals, and $t_{n-2,\,0.975}$ is the 97.5th percentile of the t distribution with $n - 2$ degrees of freedom.

The uncertainty of the scarp height was derived by error propagation of the two independent prediction uncertainties:

$$\Delta D = \sqrt{(\Delta \hat{y}_1)^2 + (\Delta \hat{y}_2)^2}.$$

Accordingly, the scarp height is expressed as:

$$D \pm \Delta D.$$

3.2. Luminescence Dating

Luminescence dating was employed to constrain both the timing of alluvial fan formation and the activity history of the GF. This technique is widely used in Quaternary geomorphological and tectonic studies to determine the formation ages of late Quaternary geomorphic surfaces and to estimate long-term fault slip rate (e.g., Wang *et al*., 2016; Gong *et al*., 2017; Ota *et al*., 2024). Quartz optically stimulated luminescence (OSL) dating was adopted as the primary chronological method. For samples inferred to be relatively old based on their greater elevation above the present riverbed and the strongly weathered condition of the terrace deposits, K-feldspar post-infrared infrared stimulated luminescence ($pIRIR_{50,225}$) dating was applied as the primary luminescence dating method.

3.2.1. Sample collection

A total of five samples for luminescence dating were collected, including four samples from surface Qf_2 and one sample from surface Qf_3 (**Fig. 1c**). No samples were collected from Qf_1 because this surface is adjacent to the modern channel and is therefore highly susceptible to fluvial disturbance and reworking. Indeed, Qf_1 is commonly difficult to distinguish from the active floodplain.

At Qf_2, four samples (GG-1 to GG-4) were collected. Although Qf_2 is presently dissected by channels into spatially separated remnants, detailed field observations and geomorphic mapping indicate that these remnants represent the same generation of alluvial-fan surface based on their morphological characteristics and relative geomorphic positions. The four samples were therefore collected from different locations on Qf_2 to constrain its depositional history and formation interval, rather than to date individual faulting events at each sampling site. Because direct sampling immediately adjacent to the G2 fault scarp was limited by land-use modification and poor exposure, sampling sites were selected where Qf_2 deposits were accessible and their geomorphic context could be reliably established. The GG-1 sampling site consists of a clast-supported deposit overlying Miocene sedimentary rock. The sample was obtained from a sand patch developed approximately 30 cm above the bedrock surface (**Fig. 2a**). Sample GG-2 was collected from a depth of ~50 cm above the bedrock, where well-developed clast imbrication indicative of fluvial transport is observed (**Fig. 2b**). Sample GG-3 was obtained at ~40 cm above the bedrock surface; the deposit at this site contains highly rounded and strongly weathered clasts (**Fig. 2c**). Sample GG-4 was collected between previously reported fault traces (G2 and G3) and represents the highest elevation among the Qf_2 sampling sites. At this location, bedrock was not exposed, and the deposit is characterized by relatively fine-grained, matrix-supported infill sediments with a low proportion of coarse clasts, in contrast to the other Qf_2 deposits (**Fig. 2d**).

One sample (MC-1) was collected from surface Qf_3 (**Fig. 2e**). Although no fault-related geomorphic marker was identified on Qf_3, MC-1 was collected to provide an independent chronological constraint on the older fan surface and thereby establish the broader chronological framework of alluvial fan development in the study area. The MC-1 age is therefore not used as a direct chronological constraint on fault displacement or slip rate estimation. Compared to Qf_1 and Qf_2, the Qf_3 deposit exhibits a higher degree of consolidation, and the clasts within the deposit are strongly weathered.

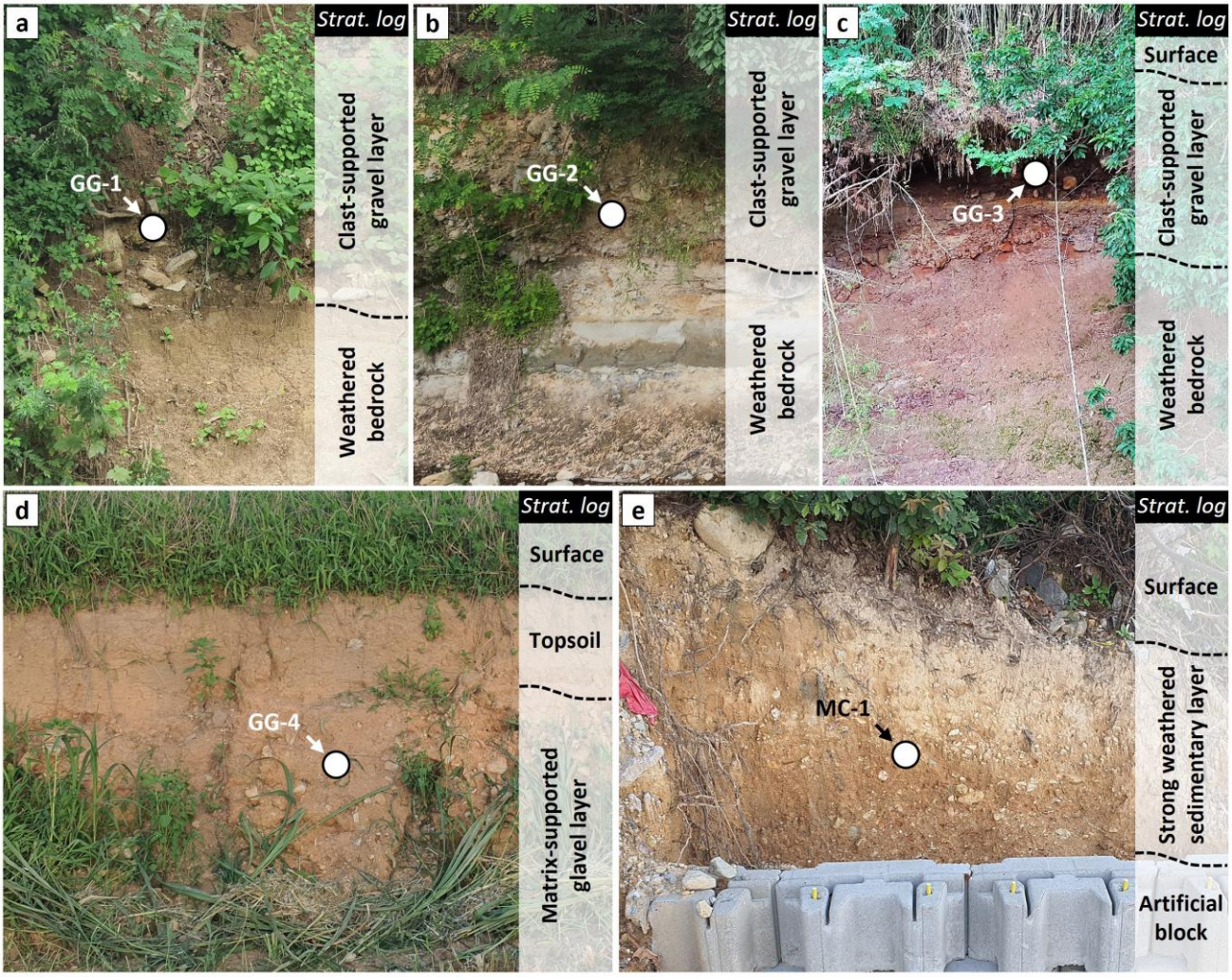


Fig. 2. *Locations of samples collected for luminescence dating. Samples in panels (a)-(d) were obtained from Qf_2, and the sample in panel (e) was obtained from Qf_3.*

3.2.2. Luminescence Dating Procedures

For luminescence dating, the 90-250 μm grain-size fraction was isolated from the samples in a subdued red-light laboratory. The bulk sediments were first wet-sieved, and the target coarse fraction was then subjected to sequential chemical treatments with 10% HCl (3h) and 10% H_2O_2 (3h) to remove carbonates and organic matter. The remaining quartz and feldspar were then separated by density with sodium polytungstate (ρ = 2.61 g·cm^{-3}). Finally, the sink fraction was etched with ~ 40 % HF for 40-60 min to obtain purified quartz. For sample MC-1, K-feldspar was recovered from the floating fraction by cleaning with 10 % HCl for 1 h, after 10 % HF etching. To verify the effective removal of feldspar from the quartz separates, an infrared (IR) stimulation test ("IR-test") was applied to both natural and β-irradiated (20 Gy) aliquots using three 8 mm aliquots per sample. The infrared stimulated luminescence (IRSL) response was consistently < 10 % of the blue-stimulated OSL signal, indicating negligible feldspar contamination in the quartz extracts.

Luminescence measurements were conducted using two automated Risø TL/OSL readers housed at the Korea Basic Science Institute. Blue light-emitting diodes (LEDs; 470 nm) were employed for quartz OSL stimulation, and infrared LEDs (870 nm) were used for K-feldspar pIRIR (post-IR IR) measurements. Photon detection was accomplished through a 7 mm Hoya U-340 filter for quartz and a blue filter pack (4 mm Corning 7-59 and 2 mm Schott BG39) for K-feldspar, mounted in front of photomultiplier tubes. Each reader is equipped with a $_{90}Sr/_{90}Y$ β source, delivering dose rates of 0.075 ± 0.004 Gy·s^{-1} and 0.157 ± 0.003 Gy·s^{-1} at the sample position. Equivalent doses (D_e) were determined using single-aliquot regenerative-dose (SAR) protocols tailored to quartz and K-feldspar (**Tables 3-4**).

Table 3. *The SAR protocol for quartz OSL D_e estimation (modified from Murray and Wintle, 2000).*

Step	Treatment	Observed
1	Give dose, D_i	-
2	Preheat (260°C for 10 s)	-
3	Blue stimulation for 40 s at 125°C	L_i
4	Give test dose, D_t	-
5	Cut-heat to 220°C for 0 s	-
6	Blue stimulation for 40 s at 125°C	T_i
7	Return to step 1	-

Table 4. *The SAR protocol for K-feldspar $pIRIR_{50,225}$ D_e estimation (Buylaert et al., 2009).*

Step	Treatment	Observed
1	Give dose, D_i	-
2	Preheat (250°C for 60 s)	-
3	IR stimulation for 100 s at 50°C	-
4	IR stimulation for 100 s at 225°C	L_i
5	Give test dose, D_t	-
6	Preheat (250°C for 60 s)	-
7	IR stimulation for 100 s at 50°C	-
8	IR stimulation for 100 s at 225°C	T_i
9	IR stimulation for 40 s at 290°C	-
10	Return to step 1	-

The $pIRIR_{50,225}$ age of MC-1 was corrected using the widely applied method of Huntley and Lamothe (2001); however, this correction method assumes that the laboratory-measured fading rate represents long-term natural fading behavior and may therefore retain model-dependent uncertainty when extrapolated to geological timescales (Kars *et al*., 2008). Environmental dose rates were derived from low-level high-resolution γ-spectrometry of the bulk sediments. Conversion of radionuclide activities to dose rates followed the updated factors of Liritzis *et al*. (2013). All dose-rate estimates were corrected for water content, using both measured and saturated values to assess the sensitivity of age estimates to moisture conditions. Attenuation of β radiation in the sediment matrix was corrected using factors from Zimmerman (1971), with a β attenuation factor of 0.93 ± 0.03 adopted for all samples. Cosmic-ray dose-rate contributions were estimated according to Prescott and Hutton (1994), accounting for burial depth, altitude, and geomagnetic latitude. For K-feldspar, the internal β dose rate from ^{40}K and ^{87}Rb was estimated following Mejdahl (1987) and Readhead (2002), assuming an internal K content of 12.5 %.

4. Results

4.1. Lineaments and Geomorphic Stratigraphy of Alluvial Fans

Across the entire study area, the mapped fault-related lineaments can be grouped into a principal fault trace, comprising five discontinuously preserved strands, and a subsidiary branch diverging from the principal trace (**Fig. 3a**). The lengths of individual strands range from approximately 240 m to 890 m. When only confidently identified strands (solid lines) are considered, the cumulative length of the principal lineament trace is ~2.64 km. When inferred strands (dashed lines) are included, the total observable length increases to ~4.56 km. These values represent the minimum along-strike extent of the GF that can be constrained from present-day geomorphic evidence.

Two fault-related lineaments were identified in the study area: a principal lineament crossing the previously reported fault sites (G1–G3) and a subsidiary branch diverging from it (**Fig. 3**). The longest continuously mapped strand of the principal trace extends for 881.8 m and exhibits a mean strike ranging from N20°–30°E, locally reaching up to N50°E. The branch lineament is 321.7 m long and trends nearly north–south, with an average strike of N0°–5°E.

These lineaments were delineated on the basis of distinct geomorphic markers, primarily fault scarps expressed on alluvial fan surfaces (**Fig. 3c–e**). In **Fig. 3**, solid red lines indicate lineaments that are confidently identified from clear geomorphic markers, whereas dashed red lines represent segments where fault-related markers are absent or obscured, particularly within incised valleys where fluvial erosion has substantially modified the original topography. Additional linear features are locally recognized both north and south of the principal lineament; however, their geometric continuity with the main trace remains uncertain. This uncertainty results from the absence of recognizable fault-related geomorphic markers within incised valley floors, where fluvial erosion has removed or obscured surface expressions of faulting.

Meanwhile, alluvial fans in the study area are subdivided into three geomorphic surfaces (Qf_1–Qf_3) (**Fig. 3a**). Although Qf_2 is presently dissected by channels into spatially separated remnants, field observations and detailed geomorphic mapping indicate that these remnants represent the same generation of alluvial-fan surface based on their morphological characteristics and relative topographic positions. All three previously reported fault sites (G1–G3) intersect the intermediate fan surface, Qf_2. Along Qf_2, the principal lineament is expressed by a clear and laterally continuous fault scarp, indicating distinct surface rupture (**Fig. 3b–e**). In contrast, no fault-related geomorphic markers are observed on the lower surface (Qf_1), which corresponds to incised valley floors adjacent to the main trace. Consequently, surface rupture associated with faulting is evident on Qf_2, whereas its presence on Qf_1 cannot be determined from geomorphic evidence. No fault-related geomorphic marker was identified on Qf_3; therefore, the age obtained from MC-1 is used to constrain the chronology of the older alluvial-fan surface rather than to directly constrain the timing of fault displacement.

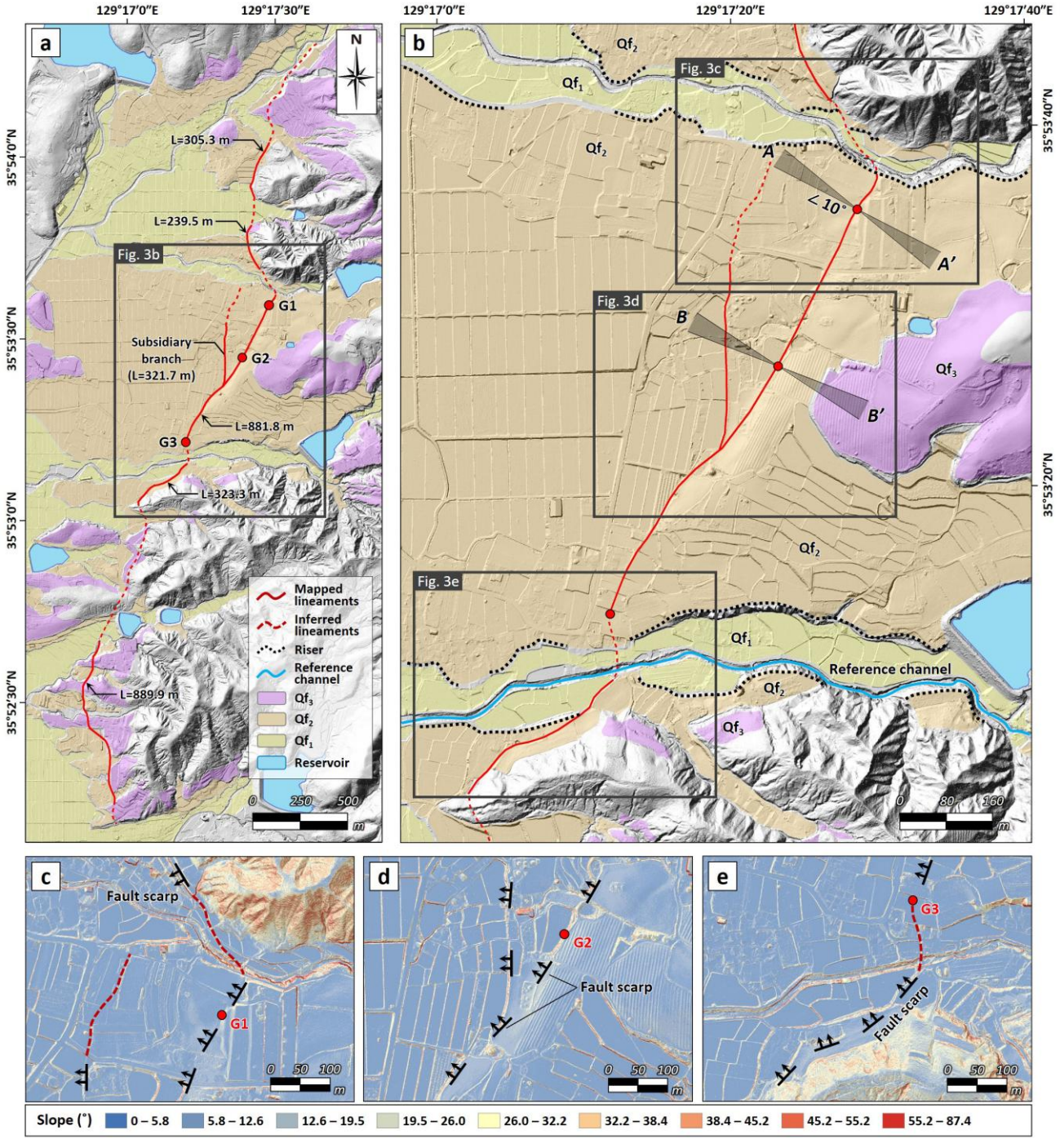


Fig. 3. *Results of geomorphic analysis. (a) Classification of alluvial fan surfaces (Qf1-Qf3) and distribution of mapped fault-related lineaments across the study area. The principal lineament consists of five discontinuous fault strands, with their individual lengths indicated, together with a subsidiary branch. Solid red lines indicate mapped lineaments confidently identified from geomorphic markers, whereas dashed red lines represent inferred lineaments where fault-related markers are absent or obscured. Black dotted lines indicate risers separating adjacent alluvial fan surfaces, and the blue line indicates the reference channel used to determine the relative elevations of the fan surfaces. (b) Detailed distribution of the principal and subsidiary lineaments and locations of topographic profiles A-A′ and B-B′ on the intermediate fan surface (Qf2). (c)-(e) Enlarged views of the G1-G3 fault sites, respectively, showing fault scarps and associated geomorphic markers. Slope maps derived from LiDAR data are used as base images in (c)-(e) to enhance the visibility of fault-related topographic expressions.*

4.2. Regression-Based Estimation of Fault Scarp Offsets

Topographic profiles across the fault at G1 (A–A′) and G2 (B–B′) exhibit abrupt steps in the mean elevation curves, corresponding to fault scarps developed on the Qf_2 surface (**Fig. 3b**, **Fig. 4a-b**). For each profile, the averaged elevation data were divided into foreland (0–150 m) and hinterland (150–300 m) segments, and linear regressions were applied independently to each segment following the procedure described in Section 3.1.

At G1, the regression lines for the two segments yield predicted elevations at the fault position (x = 150 m) of 127.66 m and 130.03 m, respectively, resulting in a vertical offset of 2.37 ± 0.17 m (95% confidence interval) (**Fig. 4c**). At G2, the corresponding predicted elevations are 117.37 m and 120.68 m, giving a vertical offset of 3.31 ± 0.24 m (95% confidence interval) (**Fig. 4d**).

These offsets represent the cumulative vertical displacement preserved on the Qf_2 surface. The close agreement between the regression fits and the averaged profiles (R^2 = 0.956–0.987) indicates that the step-like discontinuities are robust geomorphic expressions of fault-related surface rupture rather than local topographic irregularities.

4.3. Luminescence Ages of Alluvial Fan Surfaces

Luminescence dating results are summarized in **Tables 5** and **6**. Four samples (GG-1 to GG-4) were collected from the Qf_2 alluvial fan surface, whereas one sample (MC-1) was obtained from the higher Qf_3 surface (**Fig. 1c** and **Fig. 2**). Quartz OSL dating was applied to the GG samples, and $pIRIR_{50,225}$ dating was applied to the MC sample.

Quartz OSL ages from the Qf_2 surface range from 7.6 ± 0.6 ka to 34 ± 3 ka. Specifically, samples GG-1, GG-2, GG-3, and GG-4 yielded ages of 16 ± 2 ka, 24 ± 2 ka, 34 ± 3 ka, and 7.6 ± 0.6 ka, respectively (**Table 5**). These ages indicate that deposition of the Qf_2 surface occurred during the late Pleistocene to early Holocene. The Qf_3 surface is represented by sample MC-1, dated using the $pIRIR_{50,225}$ protocol. The fading-corrected age is 175 ± 6 ka (**Table 6**), placing the formation of Qf_3 in the middle Pleistocene. The luminescence ages demonstrate a clear stratigraphic ordering between geomorphic surfaces, with Qf_2 being substantially younger than Qf_3, consistent with their relative geomorphic positions.

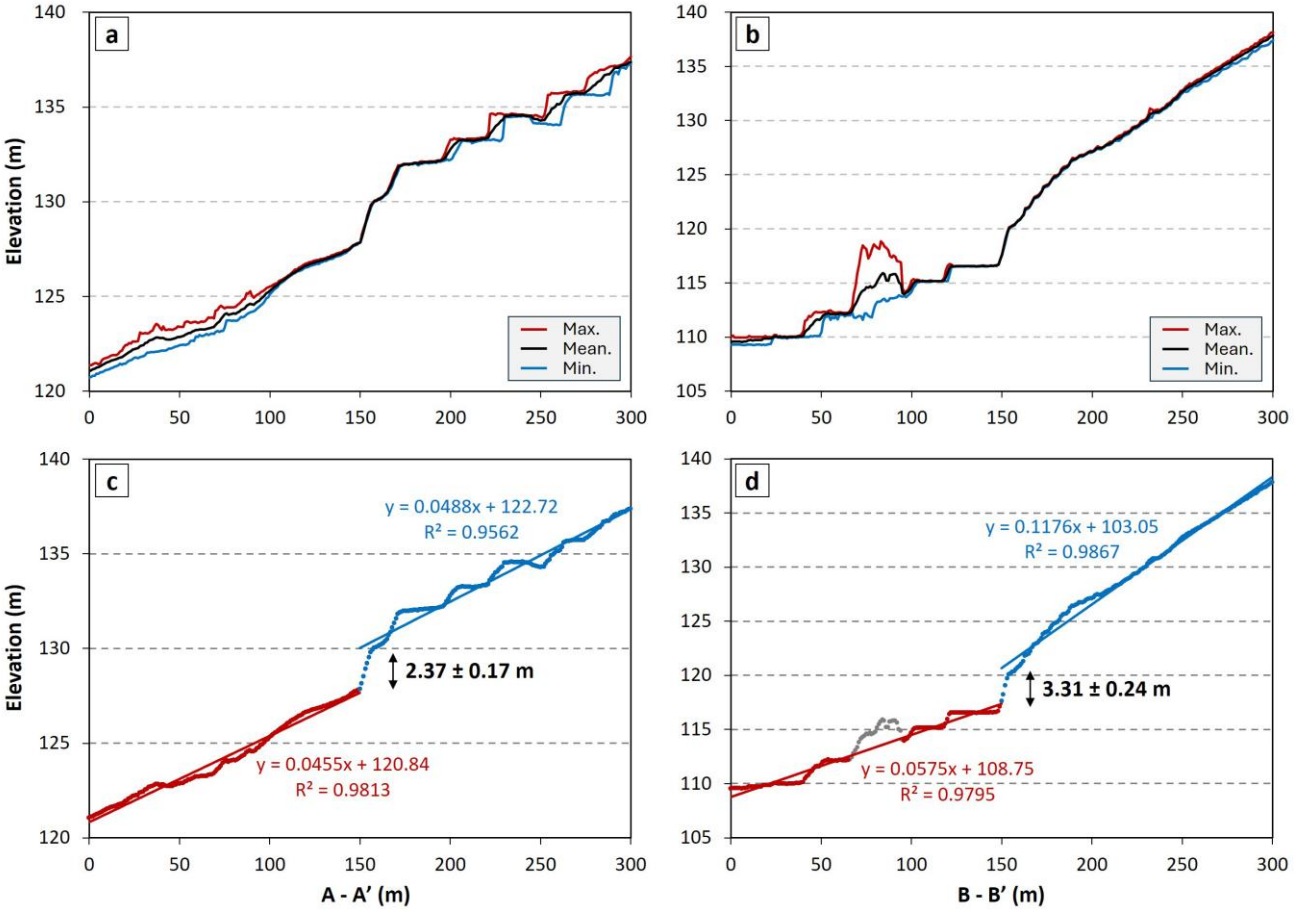


Fig. 4. *Results of topographic profile analysis. (a) and (b) show topographic profiles extracted at site G1 (profile A–A′ in Fig. 3b) and site G2 (profile B–B′ in Fig. 3b), respectively. (c) and (d) present the results of linear regression applied to the profiles in (a) and (b), with respect to the fault position.*

Table 5. *Results of quartz OSL dating.*

Sample Code	Dose Rate* (Gy/ka)	Water Content* (%)	Equivalent Dose (Gy)	n/N**	Quartz OSL age (ka, 1σ SE)
GG-1	3.64 ± 0.09	11.2	59 ± 6	16/16	16 ± 2
GG-2	3.78 ± 0.09	9.2	89 ± 7	15/16	24 ± 2
GG-3	3.87 ± 0.09	9.3	131 ± 10	15/16	34 ± 3
GG-4	2.89 ± 0.07 (2.73 ± 0.07)	17.9 (24.2)	22 ± 2	16/16	7.6 ± 0.6 (8.0 ± 0.7)

** Numbers in parentheses are those calculated based on saturated water contents.*
*** The ratio of the number of aliquots used for data analysis (n) to the total number of aliquots for luminescence measurements (N).*
! Central age ± 1σ standard error

Table 6. *Results of K-feldspar pIRIR$_{50,225}$ dating.*

Sample Code	Dose Rate* (Gy/ka)	Water Content* (%)	Equivalent Dose (Gy)	Uncorrected pIRIR$_{50,225}$ age (ka, 1σ SE)	Fading rate (g_{2days}, %/dec.)	Corrected pIRIR$_{50,225}$ age (ka, 1σ SE)	n/N**
MC-1	3.77 ± 0.08 (3.69 ± 0.08)	18.2 (21.2)	549 ± 9	145 ± 2 (149 ± 3)	2.4 ± 0.3	175 ± 6 (179 ± 5)	12/12

** Numbers in parentheses are those calculated based on saturated water contents. The internal dose rate of K-feldspar was estimated using the methods proposed by Mejdahl (1987) and Readhead (2002), assuming K content of 12.5 %.*
*** The ratio of the number of aliquots used for data analysis (n) to the total number of aliquots for luminescence measurements (N).*
! Central Age ± 1σ standard error

5. Discussion

5.1. Long-term (Late Quaternary) Slip Rate and Uncertainty from Geomorphic Markers

Slip rates estimated from geomorphic markers record cumulative offset integrated over long timescales following landform formation and therefore represent long-term tectonic behavior, particularly in slow-deforming regions (Wallace, 1977). To propagate uncertainties associated with offset and age determinations—while accounting for nonlinear relationships and asymmetric probability distributions—a Monte Carlo simulation was employed with 100,000 iterations. Slip rate estimates are summarized using median values, with associated uncertainty represented by the 16th–84th percentiles (**Fig. 5**) to avoid implicit assumptions of normality and to robustly represent the resulting probability distributions.

The chronological framework for estimating the long-term slip rate is based on the geomorphic relationship between the dated Qf_2 deposits and the displaced Qf_2 surface, rather than on direct dating of faulting at G2. Although Qf_2 is presently dissected into spatially separated remnants, detailed geomorphic mapping indicates that these remnants belong to the same generation of alluvial-fan surface. The OSL ages obtained from multiple locations are therefore used collectively to constrain the depositional history and formation interval of Qf_2. Because the fault scarp at G2 displaces this geomorphically correlated Qf_2 surface, the cumulative vertical offset is interpreted to have developed after the formation of Qf_2. Accordingly, the age-offset relationship used here provides a geomorphically constrained estimate of long-term, time-averaged deformation rather than a direct age or slip rate of an individual faulting event.

Based on this geomorphic framework, time-averaged vertical slip rates were estimated using the cumulative offset preserved on Qf_2 (3.31 ± 0.24 m; **Fig. 4d**) and the depositional ages obtained from the Qf_2 deposits (7.6 ± 0.6 ka, 16 ± 2 ka, 24 ± 2 ka and 34 ± 3 ka; **Table 5**). When the full range of Qf_2 ages is considered, the resulting median estimates range from ~0.10 to 0.44 mm/yr (**Fig. 5a–b**). These estimates differ substantially from slip rates of 0.09 to 0.1 mm/yr recalculated in this study using vertical displacement and age data reported in previous studies (Okada *et al*., 1999, 2001; Kyung, 2007). Those values were derived by re-evaluating stratigraphic evidence from the G2 site, including a cumulative vertical separation of 2.4 m in unit V (**Table 2**) and a radiocarbon age of 21,440 ± 430 yr BP (**Table 1**).

Previous trench-based estimates were derived from local stratigraphic offsets and radiocarbon ages at individual sites, whereas the present approach combines cumulative geomorphic displacement with independently dated alluvial deposits. The two approaches therefore constrain fault activity over different spatial and temporal scales (Wang *et al*., 2016; Gong *et al*., 2017; Kim *et al*., 2022; Ota *et al*., 2024) and should be regarded as complementary rather than directly equivalent. Importantly, the present geomorphic and geochronological approach provides an independent constraint on cumulative deformation that complements the event- and site-specific information obtained

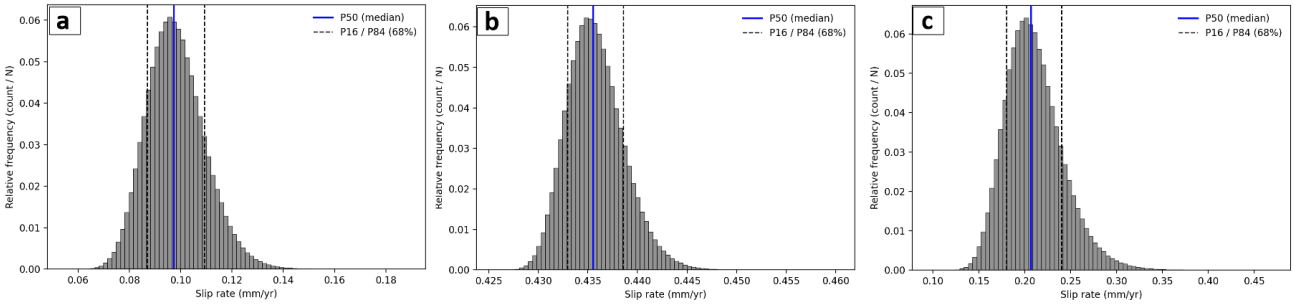


Fig. 5. *Results of Monte Carlo simulations of fault slip rates derived from the maximum cumulative offset measured on the Qf_2 surface (Fig. 4d) and OSL ages. Blue solid and dashed lines indicate the median slip rate and the 16th–84th percentiles, respectively. Panels (a), (b), and (c) show results calculated using Qf_2 formation ages of 34 ± 3 ka, 7.6 ± 0.6 ka, and 16 ± 2 ka, yielding median slip rates of 0.10 mm/yr (16th–84th percentile: 0.09–0.11 mm/yr), 0.44 mm/yr (16th–84th percentile: 0.43–0.44 mm/yr), and 0.21 mm/yr (16th–84th percentile: 0.18–0.24 mm/yr), respectively.*

from previous trench investigations. However, comparison with previous estimates also requires consideration of uncertainties in the chronological constraints. At the G1 site, ages obtained from the same sedimentary unit differ markedly: AT tephra yielded an age of ~25 ka (Suzuki *et al*., 2005), whereas radiocarbon dating produced ages ranging from 1,560 ± 60 to 14,010 ± 240 yr BP (Kyung, 2007). Kyung (2007) attributed this discrepancy to contamination by reworked organic material. Similar age reversals were also identified at the G2 and G3 sites (Okada *et al*., 1999, 2001; Inoue and Choi, 2006), where stratigraphically higher units yielded older ages than underlying units, lending further support to the interpretation of Kyung (2007) that reworked organic material affected the reliability of the radiocarbon ages.

In the present study, sample representativeness constitutes an additional source of uncertainty in constraining the depositional age of Qf_2 and, consequently, the slip rate estimates. Among the four Qf_2 samples, GG-1, GG-2, and GG-3 yielded quartz OSL ages of 16 ± 2, 24 ± 2, and 34 ± 3 ka, respectively. These samples were obtained from deposits close to the bedrock or basal unconformity and exhibit sedimentological characteristics representative of the principal Qf_2 alluvial-fan deposits (**Fig. 2a–c**). We therefore consider the 16–34 ka interval defined by GG-1 to GG-3 to provide the preferred depositional-age range for the principal phase of Qf_2 formation. The intermediate age of GG-2 (24 ± 2 ka) falls within this interval and does not affect its end-member bounds.

In contrast, GG-4 yielded a substantially younger age of 7.6 ± 0.6 ka and was collected from a shallow deposit near the present ground surface. The deposit is finer-grained and matrix-supported, with a lower proportion of coarse clasts than the deposit at the GG-1 to GG-3 sites. In addition, the site is currently used as agricultural land, and disturbance of the original sedimentary structure cannot be entirely excluded. These geomorphic and sedimentological characteristics raise the possibility that GG-4 records localized deposition or reworking after the principal phase of Qf_2 formation rather than the depositional history represented by GG-1 to GG-3. We therefore exclude GG-4 from the preferred depositional-age range while retaining it as evidence of younger sedimentation on the Qf_2 surface.

When all Qf_2 ages, including GG-4, are considered, the time-averaged vertical slip rate estimates range from ~0.10 to 0.44 mm/yr. Restricting the chronological constraint to the preferred depositional-age range of 16–34 ka reduces this range to ~0.10–0.21 mm/yr (**Fig. 5a-c**). The upper bound of the estimated slip rate is therefore particularly sensitive to whether the young GG-4 age is interpreted as representative of the principal Qf_2 depositional phase. This result emphasizes that the slip rate estimates depend not only on analytical age uncertainties but also on the geomorphic and sedimentological representativeness of the dated deposits.

Slip rate is not only a quantitative measure of crustal deformation but also a key parameter for understanding fault-slip behavior (Zechar and Frankel, 2009; Resor *et al*., 2018) and for seismic hazard assessment (Molnar and Tapponnier, 1978); accordingly, it must be evaluated with caution. Slip rates derived from individual sites inherently contain uncertainty and cannot be assumed to represent the behavior of an entire fault system (Herbert *et al*., 2014; Resor *et al*., 2018). Moreover, even within the same region, slip rate estimates may be revised as chronological interpretations are refined and analytical techniques advance. Therefore, slip rate estimates should be continuously updated through cross-validation with independent datasets, including instrumental seismicity and geodetic observations (e.g., Liu *et al*., 2021).

5.2. Possibility of Reverse-Fault Segmentation

Fault segments are commonly classified into geometric and behavior segments (Schwartz and Coppersmith, 1984; Kim *et al*., 2022). A geometric segment refers to a subdivision of a fault system based on fault geometry and spatial continuity, whereas a behavior segment describes a portion of a fault that may rupture coherently during a single earthquake. A behavior segment may correspond to a partial or complete rupture of a single geometric segment, or alternatively, to the joint rupture of two or more geometric segments (e.g., Rubin, 1996; King *et al*., 2019). Delineation

of a behavior segment requires extensive paleoseismological datasets; however, such data are inherently limited in intraplate settings such as the Korean Peninsula (Kim *et al*., 2022). In addition, studies explicitly addressing segmentation of reverse faults in intraplate settings remain scarce (McCalpin, 2009). Given these limitations, this study focuses on establishing practical criteria for geometric segmentation of reverse faults in intraplate regions and applies these criteria to the GF. Accordingly, the segmentation discussed here refers specifically to the mapped surface geometry and is not used to define the extent of a behavior segment or coseismic rupture.

The surface expression of reverse faults is often geometrically complex (e.g., Rubin, 1996; King *et al.*, 2019), largely because a single fault plane at depth commonly splays into two or more fault strands toward the surface (McCalpin, 2009; Kim *et al*., 2022). Consequently, a single subsurface fault may be mapped as multiple surface fault traces, each potentially exhibiting distinct geometric and kinematic characteristics. Distinguishing true structural discontinuities from internal fault-zone complexity is therefore critical for defining independent geometric segments. To address this issue, we define operational geometric segmentation criteria based on two parameters: (1) minimum segment length and (2) geometric separation between adjacent fault traces. These criteria provide practical mapping thresholds for distinguishing independent geometric segments from internal fault-zone complexity, rather than physical thresholds for earthquake rupture propagation.

First, the minimum length required to define an independent geometric segment was set to 1 km. This threshold is supported by two lines of evidence. (1) The minimum reported surface rupture length of reverse-fault earthquakes in intraplate regions is 1.26 km (Dawson *et al*., 2008). (2) A surface rupture length of approximately 1 km is predicted using the empirical relationships of Wells and Coppersmith (1994), assuming a minimum earthquake magnitude of M ≈ 5.0 for reverse-fault earthquakes that produced surface rupture in intraplate regions (e.g., Gordon and Lewis, 1980; Dawson *et al*., 2008; Clark *et al*., 2014; King *et al.*, 2019; Ritz *et al*., 2020; Figueiredo *et al*., 2022). These observations provide a first-order length scale for defining mappable geometric segments and are not used to infer individual earthquake rupture dimensions. Second, where multiple fault traces are identified at the surface, only those separated by a distance greater than 1 km are classified as distinct geometric segments. This threshold is based on observations of reverse-fault surface ruptures (e.g., Philip and Meghraoui, 1983; Meyer, 1991; Rubin, 1996; Boncio *et al*., 2018), in which multiple surface traces and structural complexities may occur over widths of approximately 1 km. Accordingly, closely spaced fault traces separated by less than approximately 1 km are treated as internal fault zone complexity rather than boundaries between independent geometric segments.

At the surface, the GF is expressed as a main fault trace accompanied by a subsidiary splay fault. The combined observable length of these traces is 4.56 km, and the separation between the main and subsidiary traces is ~0.25 km (**Fig. 6**). Based on the geometric segmentation criteria adopted in this study, these traces are therefore interpreted as constituting a single geometric segment (**Fig. 6**). Thus, 4.56 km represents the minimum observable geometric length of the GF based on the presently preserved surface evidence.

The total mapped length of the GF is relatively short compared to surface rupture lengths commonly reported for reverse-fault earthquakes, which often extend for several tens of kilometers (e.g., Wells and Coppersmith, 1994; Rubin, 1996). Previous studies report a single-event vertical separation of approximately 1 m (e.g., Inoue and Choi, 2006; Kyung, 2007; Choi *et al*., 2012), implying substantial coseismic displacement. The combination of a relatively short mapped length and large displacement is analogous to the "short, fat fault problem" described by McCalpin (2009), whereby the mapped fault length may not represent the full geometric extent of the fault system. However, the available geomorphic and paleoseismological evidence for the GF is insufficient to determine whether its mapped length reflects the full fault extent or whether past coseismic ruptures extended beyond the presently mapped traces. Thus, the "short, fat" relationship is considered here as an indication of uncertainty in the mapped fault extent, rather than evidence for a specific larger-scale rupture scenario.

The geometric segmentation established here therefore characterizes the presently observable surface configuration of the GF, rather than its earthquake rupture behavior. Whether the GF continues beyond its mapped extent, either at the surface or in the subsurface, remains unresolved. Further investigations of subsurface fault geometry, including geophysical surveys and drilling, are required to delineate its concealed along-strike continuation and to clarify its structural and kinematic relationships with nearby faults within the broader Ulsan Fault.

6. Conclusion

This study provides the first geomorphically constrained, luminescence-based assessment of late Quaternary slip behavior along the GF, a reverse fault located in the northern sector of the Ulsan Fault. Integrated geomorphic analysis and luminescence dating of offset alluvial fan surfaces enabled independent estimation of cumulative offset and late Quaternary time-averaged vertical slip rates (0.10–0.21 mm/yr), providing an independent perspective on fault activity in a low-strain intraplate setting.

Slip rate estimates derived from geomorphic markers represent time-averaged deformation over late Quaternary timescales and differ from values inferred from trench-based stratigraphic evidence, which reflect shorter-term or event-specific deformation. These discrepancies highlight

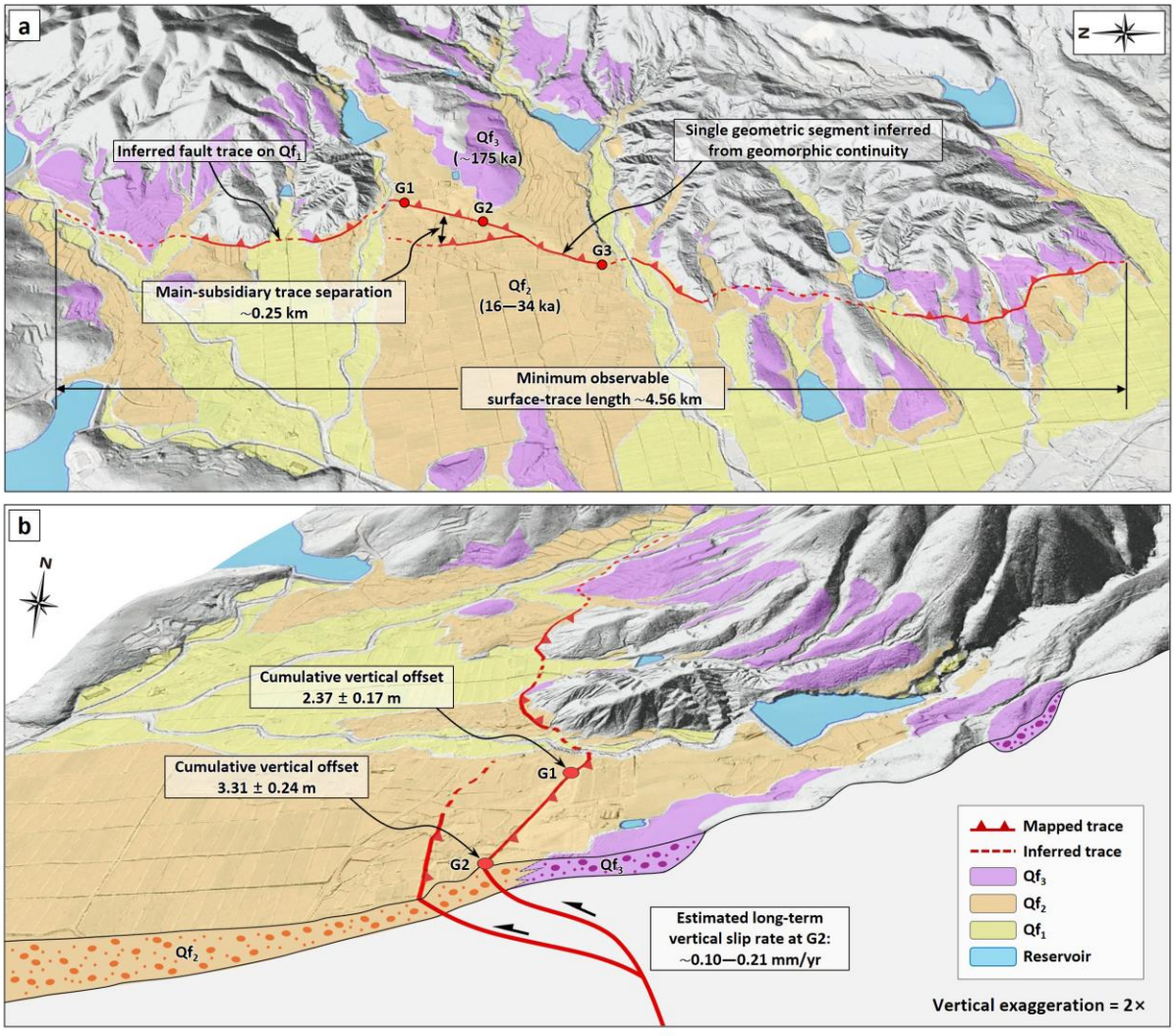


Fig. 6. *Conceptual 3D schematic of the geometric segmentation of the Galgok Fault (GF) based primarily on geomorphic continuity. This figure summarizes fault segmentation inferred from geomorphic and chronological evidence of Quaternary alluvial surfaces. (a) Oblique view showing the distribution of Qf_1-Qf_3 surfaces and mapped and inferred fault traces. Fault-related geomorphic expression is clearly preserved on Qf_2, whereas no distinct fault-related geomorphic marker is identified on Qf_3, and the fault trace across Qf_1 is inferred from the continuity of adjacent traces. The studied fault section is interpreted as a single geometric segment based on the along-strike continuity of the fault traces. (b) Oblique 3D-view illustrating cumulative vertical offsets preserved on Qf_2 surfaces, indicating progressive deformation since fan formation. The cumulative vertical offsets are 2.37 ± 0.17 m at G1 and 3.31 ± 0.24 m at G2. Based on the G2 offset and the preferred depositional-age range of Qf_2, the estimated long-term vertical slip rate is ~0.10-0.21 mm/yr. Solid and dashed lines denote mapped and inferred fault traces, respectively.*

the importance of integrating geomorphic and stratigraphic approaches when evaluating fault behavior and emphasize the need for careful consideration of geomorphic context in interpreting numerical age data.

Geometric analysis of surface fault traces indicates that the GF constitutes a single geometric segment, despite the presence of subsidiary splays. However, the relatively short mapped fault length in relation to the observed displacement suggests that the presently mapped traces may represent only the minimum observable geometric extent of the GF. Whether the fault continues beyond this mapped extent remains unresolved. Accordingly, fault segmentation inferred solely from surface geometry should be interpreted with caution in reverse-fault-dominated intraplate regions.

Overall, this study demonstrates that combining geomorphic markers with luminescence dating provides a robust framework for characterizing long-term fault behavior where paleoseismological records are limited. The results contribute to a refined understanding of reverse fault activity in southeastern Korea and provide a fundamental dataset for long-term seismic hazard assessment in regions hosting critical infrastructure.

Acknowledgment

This research was supported by a grant (2022-MOIS62-001 (RS-2022-ND640011)) from the National Disaster Risk Analysis and Management Technology in Earthquake Program funded by the Ministry of the Interior and Safety (MOIS, Korea), and by the Ministry of Education of the Republic of Korea and the National Research Foundation of Korea (NRF-2026S1A5C4021468).

References

Boncio P, Liberi F, Caldarella M and Nurminen FC, 2018. Width of surface rupture zone for thrust earthquakes: implications for earthquake fault zoning. *Natural Hazards and Earth System Sciences* 18: 241–256, DOI 10.5194/nhess-18-241-2018.

Burchfiel BC, Royden LH, van der Hilst RD, Hager BH, Chen Z, King RW, Li C, Lü J, Yao H and Kirby E, 2008. A geological and geophysical context for the Wenchuan earthquake of 12 May 2008, Sichuan, People's Republic of China. *GSA Today (The Geological Society of America)* 18(7): 4-11, DOI 10.1130/GSATG18A.1.

Buylaert JP, Murray AS, Thomsen KJ and Jain M, 2009. Testing the potential of an elevated temperature IRSL signal from K-feldspar. *Radiation Measurements* 44: 560–565, DOI 10.1016/j.radmeas.2009.02.007.

Cheong CS, Hong DG, Lee KS, Kim JW, Choi JH, Murray AS, Chwae U, Im CB, Chang CJ and Chang HW, 2003. Determination of slip rates by optical dating of fluvial deposits from the Wangsan fault, SE Korea. *Quaternary Science Reviews* 22: 1207–1211, DOI 10.1016/S0277-3791(03)00020-9.

Choi S-J, Jeon JS, Song GY, Kim HC, Kim YH, Choi BY, Chwae WC, Han JG, Ryoo CR, Seon CG, Cho MS, Kim KY, Kim YB, Lee HJ, Shin JS, Lee YS, Kee WS, Lee HK, Song YG, Kim YS, Kang TS, Hong DG and Kim SC, 2012. *Active fault map and seismic hazard map*. National Emergency Management Agency (NEMA): P205–216 (in Korean).

Clark D, McPherson A, Allen T and De Kool M, 2014. Coseismic surface deformation caused by the 23 March 2012 Mw 5.4 Ernabella (Pukatja) earthquake, central Australia: Implications for fault scaling relations in cratonic settings. *Bulletin of the Seismological Society of America* 104(1): 24–39, DOI 10.1785/0120120361.

Dawson J, Cummins PR, Tregoning P and Leonard M, 2008. Shallow intraplate earthquakes in Western Australia observed by interferometric Synthetic Aperture Radar. *Journal of Geophysical Research* 113: B11408, DOI 10.1029/2008JB005807.

Figueiredo PM, Hill JS, Merschat AJ, Scheip CM, Stewart KG, Owen LA, Wooten RM, Carter MW, Szymanski E, Horton SP, Wegmann KW, Bohnenstiehl DR, Thompson GW, Witt A, Cattanach B and Douglas T, 2022. The Mw 5.1, 9 August 2020, Sparta earthquake, North Carolina: The first documented seismic surface rupture in the eastern United States. *GSA Today (The Geological Society of America)* 32(3–4): 4–7, DOI 10.1130/GSATG517A.1.

Fournier M, Jolivet L, Davy P and Thomas J-C, 2004. Backarc extension and collision: an experimental approach to the tectonics of Asia. *Geophysical Journal International* 157: 871–889, DOI 10.1111/j.1365-246X.2004.02223.x.

Gong Z, Sun J, Zhang Z, Fu B and Jia Y, 2017. Optical dating of an offset river terrace sequence across the Karakax fault and its implication for the late Quaternary left-lateral slip rate. *Journal of Asian Earth Sciences* 147: 415–423, DOI 10.1016/j.jseaes.2017.07.013.

Gordon FR and Lewis JD, 1980. *The Meckering and Calingiri Earthquake October 1968 and March 1970*. Geological Survey of Western Australia: Perth, Australia, 1980.

Hall R, 2002. Cenozoic geological and plate tectonic evolution of SE Asia and the SW Pacific: computer based reconstructions, model and animations. *Journal of Asian Earth Sciences* 20: 353–431. DOI 10.1016/S1367-9120(01)00069-4.

Herbert JW, Cooke ML, Oskin M and Difo O, 2014. How much can off-fault deformation contribute to the slip rate discrepancy within the eastern California shear zone?. *Geology* 42(1): 71-75, DOI 10.1130/g34738.1.

Huntley DJ and Lamothe M, 2001. Ubiquity of anomalous fading in K-feldspars and the measurement and correction for it in optical dating. *Canadian Journal of Earth Sciences* 38(7): 1093-1106, DOI 10.1139/e01-013.

Inoue D and Choi W-H, 2006. The activity of the Ulsan Fault System based on marine terrace age study at southeastern part of Korean Peninsula. Central Research Institute of Electric Power Industry (CRIEPI) Report: 1-82p.

Kaneda H, Nakata T, Tsutsumi H, Kondo H, Sugito N, Awata Y, Akhtar SS, Majid A, Khattak W, Awan AA, Yeats RS, Hussain A, Ashraf M, Wesnousky SG and Kausar AB, 2008. Surface rupture of the 2005 Kashmir, Pakistan, earthquake and its active tectonic implications. *Bulletin of the Seismological Society of America* 98: 521-557, DOI 10.1785/0120070073.

Kars RH, Wallinga J and Cohen KM, 2008. A new approach towards anomalous fading correction for feldspar IRSL dating-tests on samples in field saturation. *Radiation Measurements* 43(2-6): 786-790, DOI 10.1016/j.radmeas.2008.01.021.

Kee W-S, Kim Y-H, Lee H-J, Choi D-L, Kim B-C, Song K-Y, Koh H-J, Lee SR, Hwang YY, Hwang S-H, Park K-G and Sung N-H, 2009. *South Eastern Fault Variable Research and DB Construction*. Korea Institute of Geoscience and Mineral Resources (KIGAM): 327p (in Korean).

Kim H, Synn J-H, Park C, Song WK, Park ES, Jung Y-B, Cheon D-S, Bae S, Choi S-O, Chang C and Min K-B, 2021. Korea stress map 2020 using hydraulic fracturing and overcoring data. *Tunnel & Underground Space* 31(3): 145-166, DOI 10.7474/TUS.2021.31.3.145.

Kim K-H, Ree J-H, Kim Y, Kim S, Kang SY and Seo W, 2018. Assessing whether the 2017 Mw 5.4 Pohang earthquake in South Korea was an induced event. *Science* 360(6392): 1007-1009, DOI 10.1126/science.aat6081.

Kim M-C, Jung S, Yoon S, Jeong R-Y, Song CW and Son M, 2016. Neotectonic crustal deformation and current stress field in the Korean Peninsula and their tectonic implications: a review. *The Journal of the Petrological Society of Korea* 25: 169-193, DOI 10.7854/JPSK.2016.25.3.169 (in Korean with English abstract).

Kim Y-S and Sanderson DJ, 2008. *Earthquake and fault propagation, displacement and damage zone*. In: Structural Geology: New Research: 99-117.

Kim Y-S, Son M, Choi J-H, Choi J-H and Lee H-K, 2022. *Research and Development of Active Fault of Korea Peninsula*. Ministry of the Interior and Safety (MOIS): 278-288p (in Korean).

Kim Y-S, Son M, Choi J-H, Choi J-H, Seong YB and Lee J, 2020. Processes and challenges for the production of Korean active faults map. *Journal of the Geological Society of Korea* 56(2): 113-134, DOI 10.14770/jgsk.2020.56.2.113 (in Korean with English abstract).

King TR, Quigley M and Clark D, 2019. Surface-rupturing historical earthquakes in Australia and their environmental effects: New insights from re-analyses of observational data. *Geosciences* 9: 408, DOI 10.3390/geosciences9100408.

Korea Meteorological Administration (KMA), 2012. *Historical earthquake records in Korea (2-1904)*, Yale Jeongpan: 13p (in Korean).

Korea Meteorological Administration (KMA), 2026. *Earthquake catalog of the Korean Peninsula*. Available at: https://necis.kma.go.kr (accessed 2026 January 26).

Kuwahara Y, Choi J-H, Cheon Y and Imanishi K, 2021. Dependence of earthquake faulting type on fault strike across the Korean Peninsula: Evidence for weak faults and comparison with the Japanese

Archipelago. *Tectonophysics* 804: 228757, DOI 10.1016/j.tecto.2021.228757.

Kyung JB and Lee K, 2006. Active fault study of the Yangsan fault system and Ulsan fault system, southeastern part of the Korean Peninsula. *Journal of the Korean Geophysical Society* 9(3): 219–230 (in Korean with English abstract).

Kyung JB, 2007. *Paleoseismological characteristics of the Yangsan fault zone and the Ulsan fault zone since the late Quaternary*. In: Proceeding of the 5th Symposium on the Geology of Korea, No. 3: Quaternary tectonic movements in southeastern Korea, Korea Institute of Geoscience and Mineral Resources (KIGAM): 105-117p (in Korean).

Liritzis I, Stamoulis K, Papachristodoulou C and Ionnides K, 2013. A re-evaluation of radiation dose-rate conversion factors. *Mediterranean Archaeology and Archaeometry* 13(3): 1-15.

Liu J, Ren Z, Min W, Ha G and Lei J, 2021. The advance in obtaining fault slip rate of strike-slip fault: A review. *Earthquake Research Advances* 1: 100032, DOI 10.1016/j.eqrea.2021.100032.

Ma K, Lee C, Tsai Y, Shin T and Mori J, 1999. The Chi-Chi, Taiwan earthquake: large surface displacements on an inland thrust fault. *Transactions American Geophysical Union* 80: 605–611, DOI 10.1029/99eo00405.

McCalpin JP, 2009. *Paleoseismology*, Second Edition: 315-379p., DOI 10.1016/S0074-6142(09)95005-7.

Mejdahl V, 1987. Internal radioactivity in quartz and feldspar grains. *Ancient TL* 5(2): 10-17, DOI 10.26034/la.atl.1987.119.

Meyer B, 1991. Méceanismes des Grands Tremblements de Terre et du Raccourcissement Crustal Oblique au Bord Nord-est du Tibet. Ph.D. dissertation, Paris, Université Paris: 129p.

Molnar P and Tapponnier P, 1978. Active tectonics of Tibet. *Journal of Geophysical Research* 83: 5361-5375, DOI 10.1029/JB083iB11p05361.

Murray AS and Wintle AG, 2000. Luminescence dating of quartz using an improved single-aliquot regenerative-dose protocol. *Radiation Measurements* 32: 57-73, DOI 10.1016/S1350-4487(99)00253-x.

Okada A, Takemura K, Watanabe W, Suzuki Y and Kyung J-B, 2001. Trench excavation surveys across the Yangsan and Ulsan active fault systems in the southeastern part of Korea Peninsula. *Transactions, Japanese Geomorphological Union* 22-3: 287-306 (in Japanese).

Okada A, Takemura K, Watanabe M, Suzuki Y, Kyung J-B, Chae Y-H, Taniguchi K, Ishiyama T, Kawabata D, Kaneda H and Naruse T, 1999. Trench excavation survey across the Ulsan (active) fault at Kalgok-ri, Kyongju City, Southeast of Korea. *Journal of Geography* 108(3): 276-288 (in Japanese), DOI 10.5026/jgeography.108.276.

Ota Y, Chen C-Y and Lee P-N, 2024. The Chaochou active fault in southern Taiwan: Characteristics and geomorphological significance as a reverse fault. *Journal of Structural Geology* 185: 105191, DOI 10.1016/j.jsg.2024.105191.

Park JC, Kim W, Chung TW, Baag CE and Ree JH, 2007. Focal mechanism of recent earthquakes in the southern Korean Peninsula. *Geophysical Journal International* 169: 1103-1114, DOI 10.1111/j.1365-246X.2007.03321.x.

Park J-Y, 2004. *The structural characteristics of the Tertiary basin in Gyeongju region, Korea*. Unpublished M.S. thesis, Seoul National University: 140p (in Korean with English abstract). https://s-space.snu.ac.kr/handle/10371/20913.

Park Y, Ree J-H and Yoo S-H, 2006. Fault slip analysis of Quaternary faults in southeastern Korea. *Gondwana Research* 9: 118-125, DOI 10.1016/j.gr.2005.06.007.

Philip H and Meghraoui M, 1983. Structural analysis and interpretation of the surface deformations of the El Asnam earthquake of October 10, 1980. *Tectonics* 2: 17-49, DOI 10.1029/TC002i001p00017.

Prescott JR and Hutton JT, 1994. Cosmic ray contribution to dose rates for luminescence and ESR dating: Large depths and long-term time variations. *Radiation Measurements* 23(2/3): 497-500, DOI 10.1016/1350-4487(94)90086-8.

Readhead ML, 2002. Absorbed dose fraction for ^{87}Rb β particles. *Ancient TL* 20(1): 25-28, DOI 10.26034/la.atl.2002.342.

Resor PG, Cooke ML, Marshall ST and Madden EH, 2018. Influence of fault geometry on the spatial distribution of long-term slip with implications for determining representative fault-slip rates. *Bulletin of the Seismological Society of America* 108: 1837-1852, DOI 10.1785/0120170332.

Ritz JF, Baize S, Ferry M, Larroque C, Audin L, Delouis B and Mathot E, 2020. Surface rupture and shallow fault reactivation during the 2019 Mw 4.9 Le Teil earthquake, France. *Communications Earth & Environment* 1:10, DOI 10.1038/s43247-020-0012-z.

Rizza M, Mahan SA, Ritz JF, Nazari H, Hollingsworth J and Salamati R, 2011. Using luminescence dating of coarse matrix material to estimate the slip rate of the Astaneh fault, Iran. *Quaternary Geochronology* 6: 390-406, DOI 10.1016/j.quageo.2011.03.001.

Rubin CM, 1996. Systematic underestimation of earthquake magnitudes from large intracontinental reverse faults: Historical ruptures break across segment boundaries. *Geology* 24(11): 989-992, DOI 10.1130/0091-7613(1996)024<0989:SUOEMF>2.3.CO;2.

Schwartz DP and Coppersmith KJ, 1984. Fault behavior and characteristic earthquakes: Examples from the Wasatch and San Andreas fault zones. *Journal of Geophysical Research Atmospheres* 89: 5681-5698, DOI 10.1029/JB089iB07p05681.

Sibson RH, 1985. A note on fault reactivation. *Journal of Structural Geology* 7(6): 751-754, DOI 10.1016/0191-8141(85)90150-6.

Soh I, Chang C, Lee J, Hong T-K and Park E-S, 2018. Tectonic stress orientations and magnitudes, and friction of faults, deduced from earthquake focal mechanism inversions over the Korean Peninsula. *Geophysical Journal International* 213(2): 1360-1373, DOI 10.1093/gji/ggy061.

Song CW, Kim M-C, Lim H and Son M, 2022. Geological structures and extension mode of the southwestern part (Bomun area) of the Miocene Pohang basin, SE Korea. *Korean Journal of Mineralogy and Petrology* 35(3): 235-258, DOI 10.22807/KJMP.2022.35.3.235.

Suzuki Y, Okada A, Takemura K, Kyung J-B, Kim HY, Hirouchi D, Ito A, Ooishi K, Nakamura Y, Naruse T, Kitagawa H and Watanabe M, 2005. Paleoseismic activity at the northern part of the Ulsan fault zone – Excavation study at Kalgok-ri, Kyongju city, southeast Korea. *Active Fault Research* 25: 147-152 (in Japanese with English abstract).

Tapponnier P and Molnar P, 1976. Slip-line field theory and large-scale continental tectonics. *Nature* 264: 319-324, DOI 10.1038/264319a0.

Wallace RE, 1977. Profiles and ages of young fault scarps, north-central Nevada. *The Geological Society of America* 88(9): 1267-1281, DOI 10.1130/0016-7606(1977)88<1267:PAAOTF>2.0.CO;2.

Wang D, Yin G-M, Wang X-L, Liu C-R, Han F and Du J-H, 2016. OSL dating of the late Quaternary slip rate on the Gyaring Co fault in central Tibet. *Geochronometria* 43: 162-173, DOI 10.1515/geochr-2015-0040.

Wells D and Coppersmith K, 1994. New empirical relationship among magnitude, rupture length, rupture width, rupture area, and surface displacement. *Bulletin of the Seismological Society of America* 84: 974-1002, DOI 10.1785/BSSA0840040974.

Woo J-U, Rhie J, Kim S, Kang T-S, Kim K-H and Kim YH, 2019. The 2016 Gyeongju earthquake sequence revisited: aftershock interaction within a complex fault system. *Geophysical Journal International* 217: 58-74, DOI 10.1093/gji/ggz009.

Zechar JD and Frankel KL, 2009. Incorporating and reporting uncertainties in fault slip rates. *Journal of Geophysical Research: Solid Earth* 114: B12407, DOI 10.1029/2009JB006325.

Zimmerman DW, 1971. Thermoluminescence dating using fine grains from pottery. *Archaeometry* 13(1): 29-52, DOI 10.1111/j.1475-4754.1971.tb00028.x.